# Activation of Cu(111) surface by decomposition into nanoclusters driven by CO adsorption

**Authors:** Baran Eren[1,*], Danylo Zherebetskyy[1,*], Laerte L. Patera[1,2,3], Cheng Hao Wu[1,4], Hendrik Bluhm[5], Cristina Africh[2], Lin-Wang Wang[1], Gabor A. Somorjai[1,4], Miquel Salmeron[**, 1, 6]

**Affiliations:** [1]Materials Sciences Division, Lawrence Berkeley National Laboratory, 1 Cyclotron Road,

Berkeley, California 94720, United States.

[2]CNR-IOM, Laboratorio TASC, Strada Statale 14, Km.163.5, I-34149 Trieste, Italy.

[3]Physics Department and CENMAT, University of Trieste, via A. Valerio 2, I-34127 Trieste, Italy.

[4]Department of Chemistry, University of California, Berkeley, United States.

[5]Chemical Sciences Division, Lawrence Berkeley National Laboratory, 1 Cyclotron Road, Berkeley, California 94720, United States.

[6]Department of Materials Science and Engineering, University of California, Berkeley, United States.

* These authors contributed equally to this work.

** E-mail: mbsalmeron@lbl.gov Phone: +1 510-486-6704

**Abstract**: The (111) surface of copper, its most compact and lowest energy surface, became unstable when exposed to CO gas. Scanning tunneling microscopy revealed that at room temperature in the pressure range 0.1 to 100 Torr, the surface decomposed into clusters decorated by CO molecules attached to edge atoms. Between 0.2 and a few Torr CO, the clusters became mobile in the scale of minutes. Density functional theory showed that the energy gain from CO binding to low coordinated Cu atoms and the weakening of binding of Cu to neighboring atoms help drive this process. Particularly for softer metals, the optimal balance of these two effects occurs near reaction conditions. Cluster formation activated the surface for water dissociation, an important step in the water gas shift reaction.

**One Sentence Summary:** The Cu(111) surface decomposes into nano-clusters under CO at pressures in the Torr range at room temperature, and becomes highly active for water dissociation reactions.

**Main Text:**

An extensive array of surface sensitive characterization techniques that provide structural (electron and x-ray diffraction, scanning probe microscopy, etc.) and spectroscopic (Auger electron, x-ray photoelectron, infrared, Raman, etc.) information (1-2) have revealed the structure of many crystal surfaces in their pristine clean state. Most of these studies are carried out in ultra-high vacuum (UHV), which makes it possible to control sample composition and cleanliness to better than 0.1%

of a monolayer (ML). Under realistic ambient conditions however, our knowledge is far less extensive because the most sensitive techniques utilizing electrons cannot operate in the presence of gases at pressures above ~$10^{-6}$ Torr. Of particular interest is the structure of surfaces in dynamic equilibrium with gases at near-ambient pressure and temperature (1). Under these conditions weakly bound adsorbates can be present in considerable densities, a situation that can also be achieved under vacuum, but only at cryogenic temperatures. The surface structures obtained in such rarefied conditions often represent kinetically frozen states, and may not be representative of the structure under practical operating conditions. Here we overcome this difficulty using high pressure scanning tunneling microscopy (HPSTM) (3-8), and ambient pressure x-ray photoelectron spectroscopy (APXPS) (9-10), which make possible the study of surfaces in the presence of gases up or near atmospheric pressures at room temperature and above.

Copper-based heterogeneous catalysts are used in reactions such as water gas-shift (WGS), methanol oxidation, methanol synthesis, and others (11-17). The weaker cohesive energy of Cu compared to other metals such as Pt (3.50 vs 5.84 eV) is an important factor that influences (18-19), as we will show here, its response to CO adsorption. Because of its high cohesive energy, Pt(111) is stable under CO at pressures of up to at least one atmosphere (20-21), although stepped surfaces restructure under CO due to the increased binding strength of CO at step edges (22). For Cu(111), the densest and lowest energy surface, the adsorption of CO (weaker in energy than on Pt approximately by a factor of 1.7) causes a much larger restructuring in the form of metal clusters formed by detachment of atoms from the steps. These clusters are mobile and adopt particularly stable sizes and shapes, including 3 and 19 atoms. With the help of density functional theory (DFT) calculations we explain the findings as resulting from the increased adsorption energy of CO at low coordinated Cu atoms, together with the lowering of the binding energy of the metal atoms bound to CO [experimental details of sample preparation, HPSTM imaging and methodology used in DFT calculations, are explained in detail in the supporting materials (23)]. The cluster-covered surface is stable at room temperature (in the scale of hours) after desorption of CO when the gas phase is evacuated, and that this surface is extremely active in the dissociation of water, an important step in the WGS reaction.

An image of the clean Cu(111) surface under UHV (Fig. 1A) shows micrometer scale atomic steps and a few screw dislocations are visible. After introduction of 0.1 Torr of CO in the chamber a new structure was observed along the step edges while the rest of the terrace remained atomically flat (Fig. 1B). At 0.2 Torr, the terraces became covered with nanoclusters (Fig. 1C), that increased in density with CO pressure until the clusters filled the surface (Fig. 1D and Fig. S3) (23). The CO coverage, evaluated from APXPS measurements in a different chamber under identical conditions, increased from 0.06 ML at 0.1 Torr to 0.09 ML at 0.2 Torr and to 0.16 ML at 0.5 Torr of CO (24).

The structure of the clusters formed at 0.2 Torr of CO shown in Fig. 2A. A roughly bimodal size distribution is apparent, with small clusters ~ 0.5 nm in diameter with poorly resolved triangular shape, and larger hexagonal shape clusters ~ 1.5 nm in diameter. We associate the first with three Cu atom clusters with an apparent height about half that of a monatomic step, similar to the case in UHV studies (25). The larger ones we assign to 19 atom clusters forming hexagonal closed shell structures (typically with an apparent height corresponding to a monatomic step). The 19-atom closed shell structures ("magic number" clusters) are reported to be the building blocks for the homoepitaxial Cu growth on Cu(111) (26). Sometimes the clusters contain a few more atoms (Fig. S1) (23) or come in contact with each other forming aggregates that separate again later as a result of thermal mobility, which causes the clusters to evolve spatially in the scale of

minutes, as illustrated in Fig. S2 (23). Time-lapse images show the clusters forming by splitting from step edges and growing by coalescence and accretion of smaller clusters. At 1 Torr, the clusters increased further in size and density (Fig. S3) (23). These clusters are not aggregates of CO molecules, as their height is close to that of the steps, while CO produces a contrast of only a fraction of an Ångström (27).

High-resolution images (Fig. 2, B and C) showed that the perimeters of the clusters contain bright maxima arranged in hexagonal ($C_6$) or trigonal ($C_3$) symmetries, which we attribute to CO molecules. The presence of CO bound to Cu edge atoms can be rationalized by the energy gain obtained by CO adsorption on low-coordinated Cu atoms. As discussed below, DFT predicts that 12 CO molecules, one for each atom in the periphery of the 19 atom cluster, are necessary for energetic stability, and only the molecules bound to corner Cu atoms appear bright. The three-atom clusters require three CO molecules for stability. From the known CO coverage (from APXPS), and from simple cluster counting in the STM images, we conclude that all the adsorbed CO molecules are bound to the cluster edges, leaving the rest of the surface with a negligible CO coverage below 0.01 ML.

At pressures between 10 and 100 Torr, the surface was completely covered with clusters that were larger and closer to each other, making estimation of their individual sizes difficult because of finite tip-size effects. Fig. 1D shows an example of the topography of the surface under 10 Torr of CO with clusters densely covering adjacent terraces separated by monatomic steps. Unlike the case for pressure below a few Torr, the clusters are now completely covered by CO molecules, imaged as bright spots separated by distances of $\sqrt{3}$ and 2 times the Cu atomic periodicity and aligned in directions forming 60° and 90° between them. A similar surface was also observed at 100 Torr of CO (Fig. S4). We interpret the observed STM-contrast as arising from atop site CO molecules in local (2×2)-3CO and c(4×2) geometries with coverages of 0.75 and 0.5 ML, respectively. In mixed top and bridge or hollow CO sites, the STM contrast is large only for the top sites (21, 28). The (4×4) superstructure reported at cryogenic temperatures (29), was not observed here.

The CO-promoted formation of metal clusters on Cu(111) contrasts with the case of Pt(111) where no clustering is observed, and with the stepped Pt(332) and Pt(557) surfaces, where clusters form and occupy entirely the terraces (22). The CO adsorption energy on Pt is > 1 eV, but on Cu(111) this energy is only ~ 0.5 eV. However, Cu has a much lower cohesive energy of 3.50 eV compared to the 5.84 eV of Pt (18-19). The low cohesive energy of Cu has many manifestations, such as the frizzled appearance of the steps of the clean surface at room temperature caused by kink atom diffusion (30), which was not observed on Pt.

On the Cu(111) surface, we calculated the formation energy of a Cu adatom by detachment from kink sites as 0.83 eV, indicating that on a clean surface the formation of clusters is energetically unfavorable. However, the adsorption of CO on a kink site reduces the detachment energy of CO+Cu molecule-adatom couples to 0.63 eV because of the difference in CO adsorption energy on a kink site and on a Cu adatom, which we calculated as -0.77 eV and -0.96 eV, respectively. The mobility of the Cu adatoms on (111) terraces can be predicted from the calculated potential energy surface that shows a diffusion barrier of 0.14 eV (Fig. S5) (23). This barrier decreases to 0.10 eV for the Cu+CO couple. The lowering of the binding energy of metal atoms by adsorbed CO, leading to their detachment from the steps and their higher mobility on the terrace, is known as the "harpooning" effect (31). The higher density and diffusion rate of Cu+CO couples on the surface is the reason for their coalescence into clusters.

A detailed look at the Cu clusters, colored in Fig. 2A, shows that two types of CO decoration

motifs exist, with $C_6$ and $C_3$ symmetry (Fig. 2, B and C). To explain the formation, stability, and structure of these clusters, we start by placing 6 CO molecules on the 6 corner Cu atoms of a 19 atom hexagon, plus one additional CO on the top site of the center atom. The DFT calculation for this cluster provides a CO adsorption energy of 0.83 eV on the low-coordinated corner sites, much greater than the 0.47 eV adsorption energy on the flat terrace. The adsorption energy of CO in the cluster's center is 0.47 eV, similar to the flat surface. The total energy gain from the 6 corner CO molecules (2.16 eV) is not enough to overcome the formation energy of a 19-atom cluster, which we calculated to be 3.61 eV (Table S2) (23). Adsorption of CO molecules to each Cu periphery atom (i.e., including those in the middle of each side), however, results in an energy gain averaging 0.82 eV per CO. Hence, the formation of the 19 atom cluster with 13 CO molecules is -0.59 eV (Fig. 2B), meaning that it is energetically favorable (Table S2) (23). The edge and corner CO molecules have different adsorption geometries with tilt angles of $0^o$, $26^o$, and $37^o$ with respect to the surface normal for the central, edge, and corner CO molecules, respectively.

The observation of only six bright spots at the periphery (plus the central spot) is related to the electronic structure and tunneling probability of the different CO molecules. We illustrate this by calculating the tunneling current probability using the standard Bardeen approximation (equations 2 and 3 in (23)), and the calculated partial density of states (DOS) for CO molecules on the cluster and on the tip (Fig. S6) (23). The calculation reveals that the CO molecules on the corners have indeed greater tunneling contributions than the CO molecules on the edges, qualitatively explaining the experimentally observed contrast of the STM images with the 6 bright spots plus one in the center, as shown in Fig. 2, B and D. We could explain the 3-fold symmetry of some of the 19 atom clusters by adding 3 Cu atoms at the center of the 19 atoms. These 3 low-coordinated Cu atoms, producing the bright center of the cluster images, can bind 3 additional CO molecules and distort the tilt angles of the peripheral CO molecules, as shown in Fig. 2, C and E (details are shown in (23)).

Finally, we investigated the effect of clustering on surface reactivity for the WGS reaction (i.e. $CO+H_2O \leftrightarrow CO_2+H_2$), which Cu catalyzes. Water does not adsorb on the Cu(111) surface at room temperature (Fig. 4B and (32)), whereas it dissociatively adsorbs on the more active Cu(110) surface (32). Once the gas phase CO at 1 Torr was pumped away, the STM images revealed that the Cu clusters were still present, although atomic resolution could not be achieved, likely because of the absence of CO molecules adsorbed on the tip in high vacuum (Fig. 3A). In the presence of $2\times10^{-9}$ Torr of $H_2O$, the cluster-covered surface was very active in dissociating water, as shown by the increasing oxygen peak in both the Auger electron spectra (AES) shown in Fig. 3B, and in the XPS spectra shown in Fig. 3C. The APXPS spectrum indicates that the O peak is a result of the dissociative adsorption of $H_2O$ (Fig. 4A), and that no such peak appears after experiments at 0.1 Torr of CO because clustering of the Cu did not occur at lower CO pressures (Fig. 1B and 3B). A similar effect was also observed during exposure to $CO+H_2O$ mixtures, as shown in Fig. 4A. The pristine Cu(111) surface on the other hand, not pre-exposed to CO, is inactive (Fig. 4B).

Our findings open the possibility that other soft materials (Ag, Au, Zn, etc.) can similarly undergo large reconstructions at sufficiently high pressures of CO (or other molecules). We have also demonstrated that the inactive (111) face of Cu for water dissociation, a key step in the water-gas shift reaction, becomes highly activated as a result of the CO-induced clustering. The need for this type of studies to extend our understanding of the working of catalysts under operating conditions is clear.

**Acknowledgments:** This work was supported by the Office of Basic Energy Sciences (BES), Division of Materials Sciences and Engineering, of the U.S. Department of Energy (DOE) under contract no. DE-AC02-05CH11231, through the Chemical and Mechanical Properties of Surfaces, Interfaces and Nanostructures program (FWP KC3101). It used resources of the National Energy Research Scientific Computing Center, and the Advance Light Source, which are supported by the Office of Science of the U.S. Department of Energy. The computation used resources from the Oak Ridge Leadership Computing Facility (OLCF), with time allocated by the Innovative and Novel Computational Impact on Theory and Experiment (INCITE) project.

**References:**

(1) G. A. Somorjai, Introduction to Surface Chemistry and Catalysis, Wiley-VCH New York (1999).
(2) G. Ertl, Reactions at Surfaces: From Atoms to Complexity, *Angew. Chem. Int. Ed.* **47**, 3524-3535 (2008).
(3) B. J, McIntyre, M. Salmeron, G. A. Somorjai, A Variable Pressure/Temperature Scanning Tunneling Microscope for Surface Science and Catalysis Studies, *Rev. Sci. Instrum.* **64,** 687-691 (1993).
(4) L. Österlund, P. B. Rasmussen, P. Thostrup, E. Laegsgaard, I. Stensgaard, F. Besenbacher. Bridging the Pressure Gap in Surface Science: H/Cu(111), *Phys. Rev. Lett.* **86,** 460-463 (2001).
(5) E. Laegsgaard, L. Osterlund, P. Thostruo, P. B. Rasmussen, I. Stensgaard, F. Besenbacher. A High-pressure Scanning Tunneling Microscope, *Rev. Sci. Instrum.* **72**, 3537-3542 (2001).
(6) F. Tao, D. Tang, M. Salmeron, G. A. Somorjai. A New Scanning Tunneling Microscope Reactor used for High-pressure and High-temperature Catalysis Studies, *Rev. Sci. Instrum.* **79,** 084101 (2008).
(7) F. Besenbacher, P. Thostrup, M. Salmeron. The Structure and Reactivity of Surfaces Revealed by Scanning Tunneling Microscopy, *MRS Bulletin*, **37,** 677-681 (2013).
(8) C. T. Herbschleb *et al*, The Reactor STM: Atomically Resolved Scanning Tunneling Microscopy under High-Pressure, High-Temperature Catalytic Reaction Conditions, *Rev. Sci. Instrum.* **8**, 083703, (2014).
(9) M. Salmeron, R. Schlögl, Ambient Pressure Photoelectron Spectroscopy: A New Tool for Surface Science and Nanotechnology, *Surf. Sci. Rep.* **63**, 169-199 (2008).
(10) M. Salmeron, Physics and Chemistry of Material Surfaces under Ambient Conditions of Gases and Liquids: What's New? *MRS Bulletin*, **38**, 650-657 (2013).
(11) K. Klier, *Methanol Synthesis, in Advances in Catalysis*, D. D. Eley, H. Pines, P. B. Weisz, Eds. (Academic Press 31, 1982), pp. 243.
(12) D. S. Newsome, The Water-Gas Shift Reaction, *Catal. Rev.* **21,** 275-318 (1980).
(13) J. Szanyi, D. W. Goodman, Methanol Synthesis on a Cu(100) Catalyst, *Catal. Lett.*, **10**, 383-390 (1991).
(14) J. Yoshihara, C. T. Campbell, Methanol Synthesis and Reverse Water–Gas Shift Kinetics over Cu(110) Model Catalysts: Structural Sensitivity, *J. Catal.* **161**, 776-782 (1996).
(15) M. Behrens *et al*, The Active Site of Methanol Synthesis over Cu/ZnO/Al2O3 Industrial Catalysts, *Science* **336**, 893-897 (2012).
(16) G. A. Olah, Towards Oil Independence through Renewable Methanol Chemistry, *Angew. Chem. Int. Ed*. **52,** 104-107 (2013).
(17) M. Behrens. Heterogeneous Catalysis of CO2 Conversion to Methanol on Copper Surfaces,

*Angew. Chem. Int. Ed.* **53**, 12022-12024 (2014).
(18) K. Kabme, Cohesive Energy of Noble Metals, *Phys. Rev.* 99, 419-422 (1955).
(19) C. Kittel, *Introduction to Solid State Physics 8th Edition* (John Wiley & Sons, Hoboken, NJ, 2005) pp. 50.
(20) S. R. Longwitz, J. Schnadt, E. K. Vestergaard, R. T. Vang, I. Stensgaard, H. Brune, F. Besenbacher, High-Coverage Structures of Carbon Monoxide Adsorbed on Pt(111) Studied by High-Pressure Scanning Tunneling Microscopy. *J. Phys. Chem. B* **108**, 14497-14502 (2004).
(21) D. Tang, K. S. Hwang, M. Salmeron, G. A. Somorjai, High Pressure Scanning Tunneling Microscopy Study of CO Poisoning of Ethylene Hydrogenation on Pt(111) and Rh(111) Single Crystals, *J. Phys. Chem. B* **108**, 13300-13306 (2004).
(22) F. Tao, S. Dag, L. W. Wang, Z. Liu, D. R. Butcher, H. Bluhm, M. Salmeron, G. A. Somorjai, Break-Up of Stepped Platinum Catalyst Surfaces by High CO Coverage. *Science* **327**, 850-853 (2010).
(23) See supplementary materials in Science Online
(24) B. Eren, L. Lichtenstein, C. H. Wu, H. Bluhm, G. A. Somorjai, M. Salmeron, Reaction of CO with Pre-adsorbed Oxygen on Low-Index Copper Surfaces: An Ambient Pressure XPS and STM Study, *J. Phys. Chem. C* **119,** 14669-14674 (2015).
(25) J. Lagoute, X. Liu, F. Fölsch, Link between Adatom Resonances and the Cu(111) Shockley Surface State. *Phys. Rev. Lett.* **95**, 136801 (2005).
(26) O. V. Lysenko, V. S. Stepanyuk, W. Hergert, J. Kirschner, Mesoscopic Relaxation in Homoepitaxial Metal Growth, *Phys. Rev. Lett.* **89**, 126102 (2002).
(27) M. Mehlhorn, H. Gawronski, K. Morgenstern, Diffusion and Dimer Formation of CO Molecules Induced by Femtosecond Laser Pulses, *Phys. Rev. Lett.* **104**, 076101 (2010).
(28) H. J. Yang, T. Minato, M. Kawai, Y. Kim, STM Investigation of CO Ordering on Pt(111): From an Isolated Molecule to High-Coverage Superstructures, *J. Phys. Chem. C* **117,** 16429-16437 (2013).
(29) L. Bartels, D. Meyer, K. H. Rieder, The Evolution of CO Adsorption on Cu(111) as Studied with Bare and CO-functionalized Scanning Tunneling Tips, *Surf. Sci. Lett.* **432**, L621-L626 (1999).
(30) M. Poensgen, J. F. Wolf, J. Frohn, M. Giesen, H. Ibach, Step Dynamics on Ag(111) and Cu(100) Surfaces. *Surf. Sci.* **274**, 430-440 (1992).
(31) M. M. Waldrop, The 1985 Nobel Prize In Chemistry, *Science* **234**, 673-674 (1986).
(32) S. Yamamoto, K. Andersson, H. Bluhm, G. Ketteler, D. E. Starr, T. Schiros, H. Ogasawara, L. G. M. Pettersson, M. Salmeron, A. Nilsson, Hydroxyl-Induced Wetting of Metals by Water at Near-Ambient Conditions, *J. Phys. Chem. C* **111**, 7848–7850 (2007).

**Figures:**

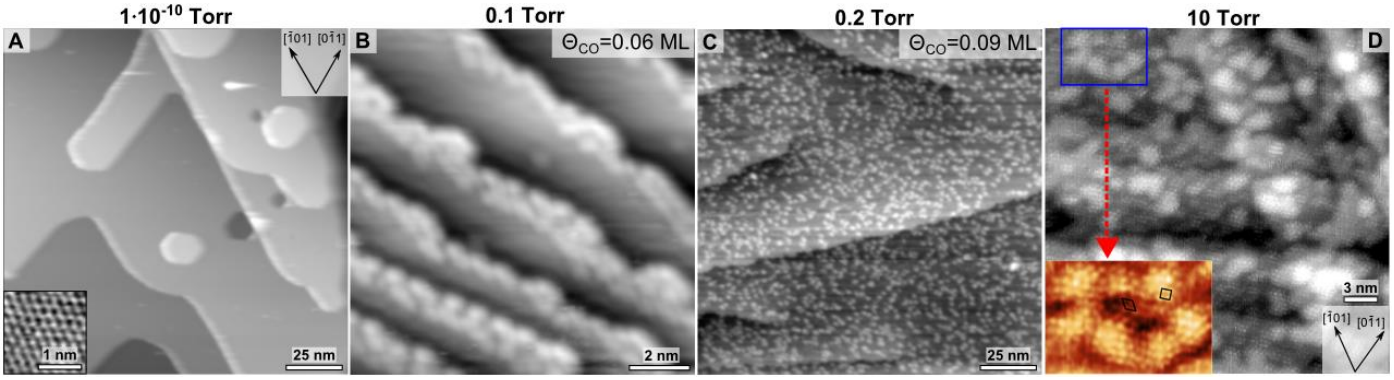


**Figure 1 STM images of Cu(111) showing clusters filling the terraces as a function of ambient CO pressure. (A**) In UHV [$V_b$= -2.4 V; $I_t$=0.1 nA]; bottom inset: atomically resolved image [$V_b$= 0.2 V; $I_t$= 1 nA]; (**B**) under 0.1 Torr of CO clusters form at steps edges [$V_b$= -2.5 V; $I_t$=0.2 nA]; (**C**) under 0.2 Torr of CO clusters form on the terraces [$V_b$= 1.85 V; $I_t$= 0.5 nA]. CO coverages in **(B)** and **(C)** are shown in the insets, as determined from the APXPS peak intensities; **(D)** under 10 Torr of CO [$V_b$= 0.15 V; $I_t$= 0.8 nA]. A high density of clusters with adsorbed CO molecules (expanded in the inset) covers completely the surface. The bright spots, due to CO on top sites, form (2×2)-3CO and c(4×2) unit cells. Scale bar is 25 nm for **(A)** and **(C**), 2 nm **(B)**, 25 nm **(C),** and 3 nm for **(D)**.

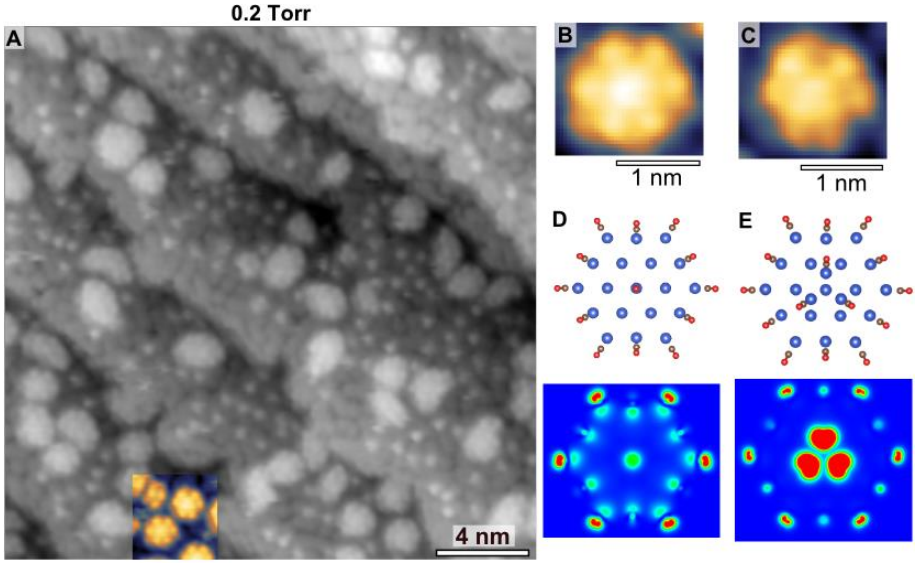


**Figure 2 STM images, ball models and simulated contrast images of Cu clusters at 0.2 Torr with hexagonal and trigonal symmetries. (A)** STM image [$V_b$= -1.5 V; $I_t$=0.2 nA]. (**B)** and **(C)** are images of the two types of clusters with $C_6$ or $C_3$ symmetry colored in **(A).** The bright center of the cluster in **(B)** is due to a CO molecule, and to a cluster of 3 Cu atoms decorated by CO in

**(C)**. **(D)** 19 atom cluster model from DFT calculations and simulated STM image ($V_b$=-2.7 V) of the cluster in **(B)**. **(E)** DFT optimized model and simulated STM image ($V_b$=-2.7 V) of the cluster in **(C)**. Images are simulated with a CO-terminated tip and using a higher bias (in absolute values) than the experimental value, because the +U correction, used to match the experimental CO-binding energy on the flat surface.

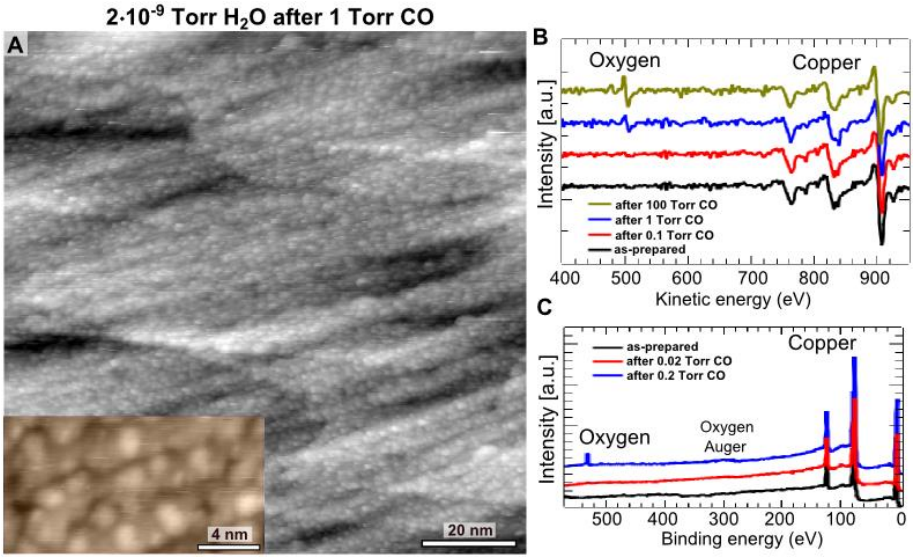


**Figure 3 STM images and AES spectra taken after evacuation the CO gas phase. (A)** STM images show that the Cu clusters remain on the surface in the presence of $2\times10^{-9}$ Torr of water 0.5 hours after evacuation [$V_b$= 0.5 V; $I_t$= 0.5 nA]. Expanded image in inset [$V_b$= 1.5 V; $I_t$= 0.2 nA]. **(B)** Auger electron spectra after evacuation of the gas phase CO from different initial pressures. The dissociative adsorption of $H_2O$ on the cluster-covered surface is evident from the increasing intensity of the O peak. (**C**) Similar observation using XPS in the Synchrotron chamber.

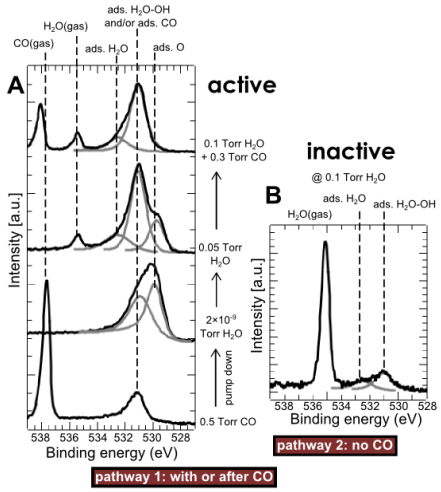


**Figure 4 APXPS experiments of $H_2O$ adsorption on Cu(111), with and without pre-adsorption of CO. (A)** $H_2O$ adsorption after CO-induced morphological changes. From bottom: under 0.5 Torr of CO; after pump down to $2\times10^{-9}$ Torr, mostly containing water (mass spectra

shown in Fig. S8 (23)); under 0.05 Torr of water; and (top) under 0.4 Torr of a 3:1 gas mixture of CO and $H_2O$. Water dissociation is activated by the large increase of low-coordinated sites produced by the CO-induced nano-cluster formation. In the presence of both water and CO (top), only OH and $H_2O$ species are observed due to the efficient reaction of CO with atomic O (24). **(B)** APXPS of a pristine Cu(111) (i.e., not exposed to CO) in the presence of 0.1 Torr of $H_2O$. The weak adsorption peaks of $H_2O$ and OH (compare with top two spectra in **(A)**), probably arise from adsorption on the defect sites.


# Supplementary Materials for

## Activation of Cu(111) Surface by Decomposition into Nanoclusters driven by CO Adsorption

Baran Eren, Danylo Zherebetskyy, Laerte L. Patera, Cheng Hao Wu, Hendrik Bluhm
Cristina Africh, Lin-Wang Wang, Gabor A. Somorjai, Miquel Salmeron*

*correspondence to: mbsalmeron@lbl.gov

**This PDF file includes:**

## Methods

Experimental Methods

The HPSTM measurements were performed in constant current mode, with Pt/Ir tips at room temperature with a custom-built STM housed in a high pressure cell. Tunneling parameters are indicated for each image in the figures, with the bias voltage applied to the sample. The Cu(111) sample was cleaned by repeated cycles of $Ar^+$ sputtering (20 min, 1 keV) and annealing at 550 °C (10 min). Auger Electron Spectroscopy (AES) was used to monitor the chemical composition before and after HPSTM experiments.

CO gas was leaked into the chamber from an initial base pressure of $1 \cdot 10^{-10}$ Torr range, after passing through a carbonyl trap at 240 ºC to prevent nickel contamination (Fig. 3B). Hydrocarbon contamination was below 0.1 ML, even after measurements at 100 Torr of CO. The pressure was measured with MKS722A Baratron capacitance and Granville Phillips 275 Convectron Pirani pressure gauges.

In addition to HPSTM, APXPS experiments were performed at the BL 11.0.2 endstation of the Advanced Light Source, the Berkeley Lab Synchrotron Facility. Photon energies of 275 eV for Cu 3p, 490 eV for C 1s, and 735 eV for O 1s were used to produce photoelectrons with kinetic energies around 200 eV in all cases. The area ratio of O 1s to Cu 3p peaks after Gaussian-Lorentzian fitting was used to determine the CO coverage ($\theta_{CO}$) in the pressure range of 0.1-0.5 Torr of CO. Detailed information about the APXPS experiments can be found elsewhere (24).

Theory

We computed the energies of various structures suggested by the experimental images. All geometry optimizations were performed within the frame of DFT using the VASP software package (33). The projector augmented wave method was utilized to construct the basis set for the one-electron wave functions with a plane-wave basis set with a cut-off energy of 420 eV (34). Cu(111) was modeled by slabs of 4 atomic layers separated by a 12 Å of vacuum to exclude surface-surface interactions. A 3×3×1 Monkhorst-Pack k-point grid is used to model the nanostructured surface whose linear dimensions are 7×7×4. A 9×9×1 k-point grid was used in a 3×3×4 slab for finding an optimal computational approach for correct CO adsorption. The energy convergence was established at $10^{-5}$ eV, while the force convergence was set at $5 \times 10^{-3}$ eV/Å.

Among the various functionals tested and applied to the 3×3×4 slab, the PBE+U approach with U=6 eV for C and O atoms provided the best agreement with experiment, predicting CO adsorption on top-sites for Cu(111), and an adsorption energy of -0.47 eV, in agreement with experiment (29, 35). The PBE+U functional was also used for the nanocluster calculations. The energy per atom in a Cu extra-layer (3×3×5 slab) was found to be -3.73 eV, slightly smaller than the atomic energy of -3.96 eV in the Cu bulk, which is in agreement with experimental cohesive energy of -3.50 eV/atom (18-19). Although PBE+U provide results in agreement with experiments for the surface-molecule interaction, it lacks the attractive intermolecular van der Waals interaction that plays a role in the clustering. The formation energies were calculated as:

$$E_{Form} = E_{tot} - E_{slab} - N_{Cu} \cdot E_{Cu}^{extra} - N_{CO} \cdot \left(E_{CO}^{gas} + E_{CO}^{ads}\right) + E_{CO}^{vdW} \qquad (1)$$

where $E_{tot}$ is the total energy of the system, $E_{slab}$ the energy of the bare slab, $N_{CO,Cu}$ the number of CO molecules and Cu atoms in the cluster, $E_{CO}^{gas}$ and $E_{CO}^{ads}$ are gas-phase and slab adsorption energies of CO, $E_{CO}^{vdW}$ is the Van der Waals interaction of the molecules on the slab. We should note that although we use the adsorption energy at low coverage (-0.47 eV), at higher coverages the CO binding to Cu becomes weaker (35), making cluster formation even more favorable.

The calculated adsorption energy of CO molecules on the Cu(111) step is -0.72 eV, in agreement with the reported experimental value of -0.70 eV (36). Van der Waals parameters for intermolecular interaction were chosen such that they qualitatively reproduce the experimental coverage dependent activation energy of CO on the Cu(111) steps (35).

**Supplementary Text**

Larger Clusters at 0.2 Torr

Fig. S1 shows images of different type of clusters observed at 0.2 Torr. Most of the clusters consist of 19-atoms and 3-atom clusters, sometimes with extra atoms attached to them as described in the main text.

STM temporal evolution

As discussed in the main text, under 0.2 Torr of CO, two-dimensional clusters with a rough bimodal distribution were formed over the Cu(111) surface. The STM time-lapse images in Fig. S2 show examples of cluster formation and coalescence events. Small clusters, with dimensions consistent with 3 Cu atom aggregates, show high mobility manifested also by the presence of dashes in the images. In Fig. S2 (a-c), arrows highlight different small clusters diffusing and coalescing into larger clusters, a behavior characteristic of Ostwald ripening (37).

Red circles in Fig. S2 (a-c) highlight the formation of larger clusters: Between (a) and (b), a small Cu cluster detaches from the step and coalesces into a bigger one. In (c), upon further attachment of materials, the cluster splits in two parts, enabling higher energy gain through CO adsorption to the edges.

Surface at 1 Torr of CO

When the pressure is increased from 0.2 Torr to 1 Torr, the cluster size and density increases, as shown in Fig. S3.

Surface structure under 10 and 100 Torr of CO

At CO pressures of 10 Torr and higher, the surface is completely filled with clusters. Topographic and corresponding derivative mode images (to enhance the resolution) are shown (Fig. S4).

DFT calculation details

The diffusion barrier of a Cu adatom on Cu(111) surface (Fig. S5) decreases from 0.14 eV to 0.10 eV upon formation of a Cu+CO adatom-molecule couple. CO attracts valence electrons of Cu adatom such that the Cu adatom loses $0.3e^-$ accordingly to Bader charge analysis. This is known as the "harpooning" effect (31).

Simulation of STM images

Our calculations show that the clusters should at least contain 12 CO molecules on their low-coordinated edges for stability. However, STM images show only six bright spots at the periphery plus one additional central bright spot. We believe that this is related to differences in the electronic structure and tunneling probability for CO molecules adsorbed on different sites of the cluster. To verify this we calculated the tunneling probability using the standard Bardeen formula (38):

$$I = \frac{4\pi e}{\hbar}\int_0^{eV} \rho_s(E_F - eV + \varepsilon)\rho_T(E_F + \varepsilon)|M|^2 d\varepsilon \,, \quad (2)$$

where $\rho_S(E)$ and $\rho_T(E)$ are the DOS of the surface and the tip. *M* is the tunneling matrix element:

$$M = \frac{\hbar}{2m}\int \left(\chi^* \frac{\partial \psi}{\partial z} - \psi \frac{\partial \chi^*}{\partial z}\right) dS \,, \quad (3)$$

with $\psi$ and $\chi$ being the wave functions of the surface and the tip.

These formulas show that the tunneling current is proportional to the overlap of wave functions of the tip and the sample CO molecules, weighted by the DOS. With this assumption, we calculated the partial DOS for the 13 CO molecules on a 19 atom cluster (Fig. S6). The DOS shows unoccupied and occupied spectral regions, with the CO molecules on the hexagonal corners exhibiting two maxima in the unoccupied region that can facilitate larger overlap with the tip DOS than the CO molecules on the edges.

Due to inevitable tip-surface contacts, and the high CO pressure in the Torr range, we model the STM-tip as Cu35-pyramid with a single CO termination. The applied sample bias will shift the Fermi level of the sample relative to the tip and the electron tunneling current is then determined by the regions with largest DOS-overlap.

The integrated charge densities near the two regions (-2.7 eV and +2.1 eV) qualitatively explain the experimentally observed contrast of the STM images with the 6 bright spots plus one in the center, as shown in Fig. 2. Note that calculated and experimental biases are different, because we applied U=+6 eV correction for the CO adsorption on top-sites.

Some clusters show a 3-fold symmetry with a bright triangle in the center (Fig. 2C). The orientation and dimensions of the triangle show that its corners are on fcc sites relative to the underlying atomic layers. Since CO molecules preferably adsorb on top of the under-coordinated Cu atoms, we model this triangle by adding 3 Cu atoms at the center on top of the 19 atoms (Fig. 2E). This central 3Cu-3CO triangle reduces $C_6$ symmetry to $C_3$ symmetry, due to intermolecular repulsion. The hexagon edges near the triangle corners are longer (6.864 Å) than the edges near the triangle edges (6.810 Å). The contrast between

these two types of hexagon edges can be more pronounced under applied electric field. The integrated charge density around -2.7 eV and +2.1 eV (Fig. S7) qualitatively explains the $C_3$ symmetry.

We should mention that charge density integration around other energies does not show such a clear distinction between all CO molecules, in line with the experimental observation that the highest hexagonal symmetry contrast is observed at certain applied biases, while for other biases the contrast is reduced and the hexagons become smeared into large bright blobs.

APXPS:

APXPS experiments were performed in order to measure CO coverages, calibrate AES data, and investigate CO+$H_2O$ co-adsorption.

Fig. 3B shows the AES spectra obtained after evacuation of the CO from the ambient pressure chamber. Similar to the AES observations, no oxygen peaks due to reaction with background water ($p \cong 2\times10^{-9}$ Torr) are observed if the Cu crystal had been exposed to CO at pressures below 0.2 Torr, where no cluster formation and detachment occurred (Fig. 3C). However, after exposure of the Cu crystal to pressures above 0.2 Torr, when cluster formation occurs, water dissociates readily on the highly reactive cluster covered surface (Fig. 3C).

Fig. 4A shows several spectra. As in previous work, chemisorbed CO produces a peak at 531.1 eV (24). Atomically adsorbed oxygen produces peaks around 529.8-529.9 eV (24), and surface hydroxide-water mixtures produce peaks near 531 eV (32). There is no lattice oxygen in the form of $Cu_2O$ (this peak is at 530.2-530.4 eV (41)). Molecular water peak is observed around 532.5 eV (32). Gas phase CO and $H_2O$ peaks are both above 535 eV (the exact positions depend on the work function of the sample and analyzer). CO and $H_2O$-OH mixture peaks are difficult to distinguish as they have very close binding energies, but we know that no adsorbed CO stays on the surface at room temperature in the absence of gas phase CO. As can be seen, after pumping the CO gas phase, water derived peaks at 531 eV, as well as atomic oxygen peaks appear, indicative of dissociative adsorption of water. Molecular water is observed when its partial pressure becomes higher that a few milliTorr. The addition, CO reacts and removes all the chemisorbed oxygen (top spectrum) due to the efficient CO+O→$CO_2$ reaction (24, 41). As in ref. (32), on a flat Cu(111) surface $H_2O$ and OH adsorption is negligible (Fig. 4B).

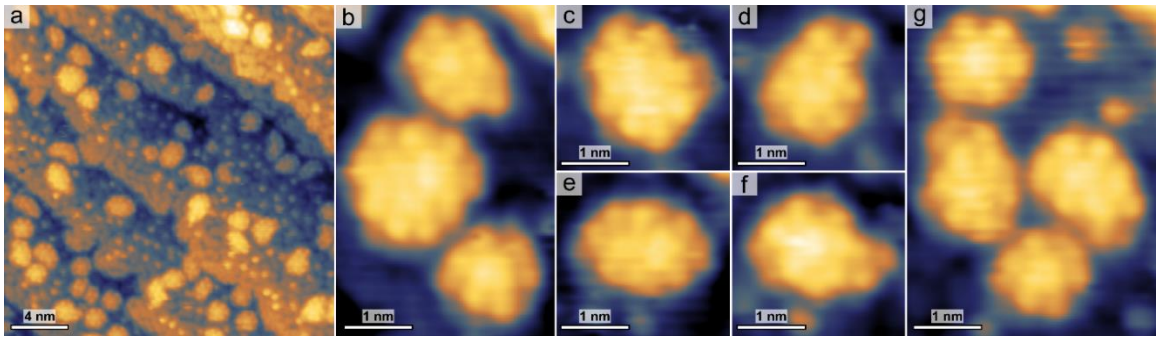


**Fig. S1.** (b-g) Different clusters observed in (a). In all of the clusters, the edges are decorated by maxima due to CO molecules. Only the corner molecules have high contrast in the STM images [$V_b$= -1.5 V; $I_t$=0.2 nA].

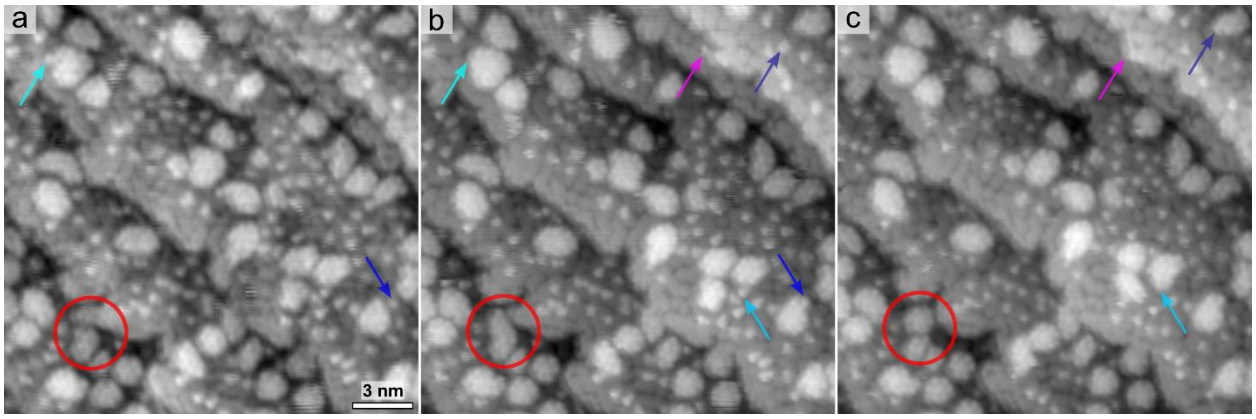


**Fig. S2.** Evolution of Cu(111) surface under 0.2 Torr of CO at RT. Cluster formation stages are highlighted with red circles. Arrows show cluster ripening. Time between displayed frames: ~180 s [$V_b$= -1.5 V; $I_t$= 0.2 nA].

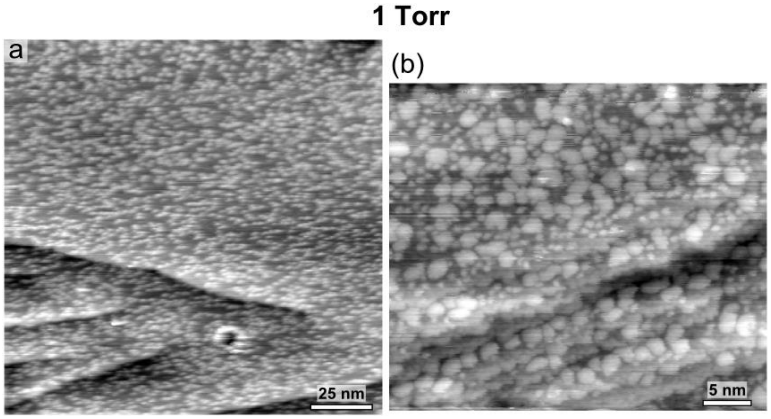


**Fig. S3.** STM image at 1 Torr of CO. The number of 3-atom clusters decreases substantially while larger clusters form on the surface Imaging parameters: [$V_b$= 0.9 V; $I_t$= 0.2 nA] in (a), [$V_b$= -1.15 V; $I_t$= 0.2 nA] in (b).

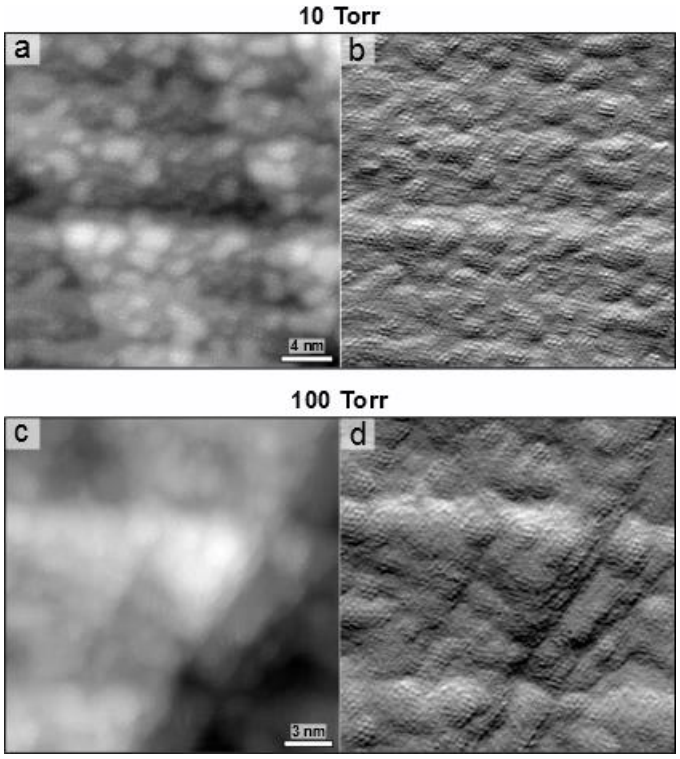


**Fig. S4.** CO induced cluster formation on Cu(111). STM images of CO covered Cu clusters under (a) 10 Torr of CO [$V_b$= 0.15 V; $I_t$= 0.8 nA] and (c) 100 Torr of CO [$V_b$= 0.15 V; $I_t$= 1.1 nA]. (b) and (d) are derivative images of (a) and (b), respectively.

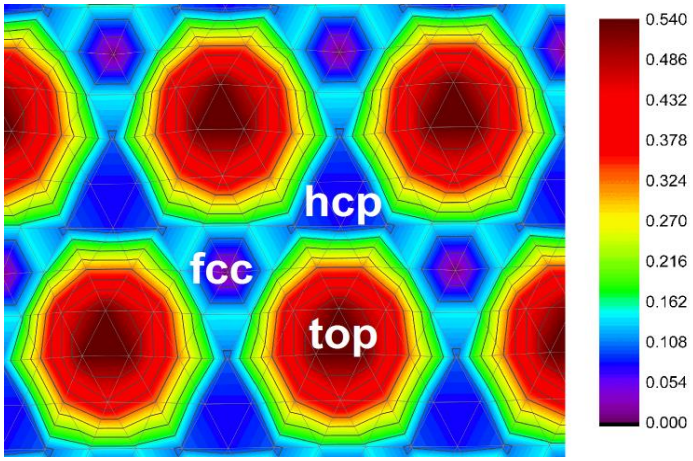


**Fig. S5.** Top view of the potential energy surface for the Cu adatom on Cu(111) surface. The smallest diffusion barrier is 0.14 eV for Cu hopping from fcc to hcp sites. The bar shows the color-coded relative energies in eV.

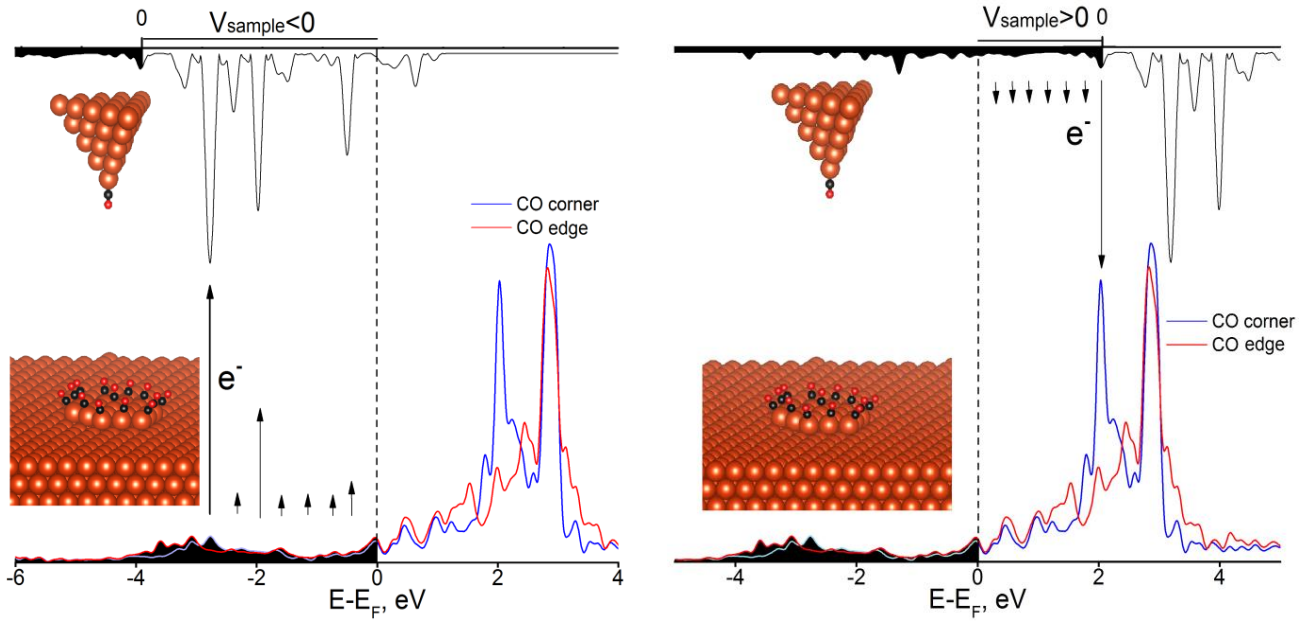


**Fig. S6.** Partial DOS for CO on a pyramidal $Cu_{35}$ tip (upside down, upper curve), and for CO adsorbed on the corner (bottom blue curve) and edges (bottom red curve) of the $C_6$ hexagonal cluster with and applied sample bias of left: -2.7 eV and right: +2.1 eV. The arrows show the largest electron tunneling channels due to the convolution of the sample and tip charge densities.

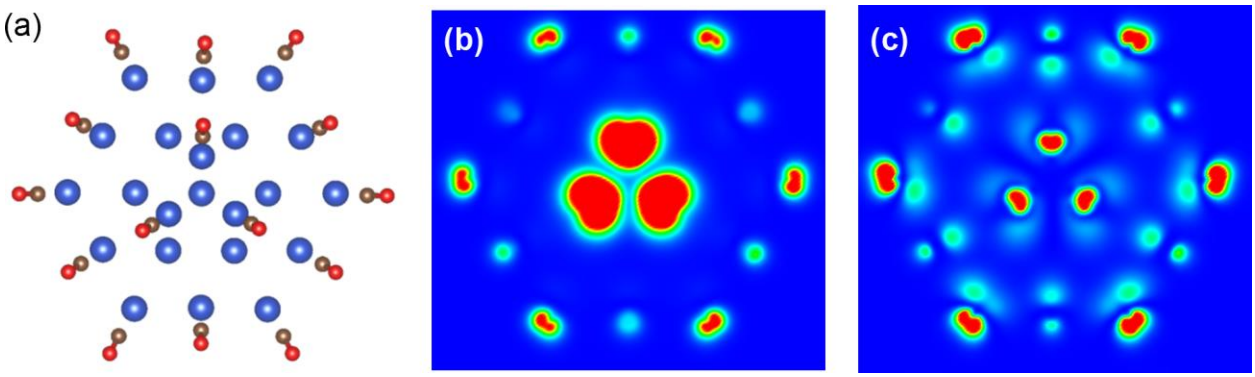


**Fig. S7.** Model for the $C_3$ hexagonal cluster with a favorable formation energy: (a) ball model (Cu-blue, C-brown atoms, O-red) of a $Cu_{22}$ cluster with 15 adsorbed CO molecules, (b) and (c) show the top views of the integrated charge density around -2.7 eV and +2.1 eV, respectively.

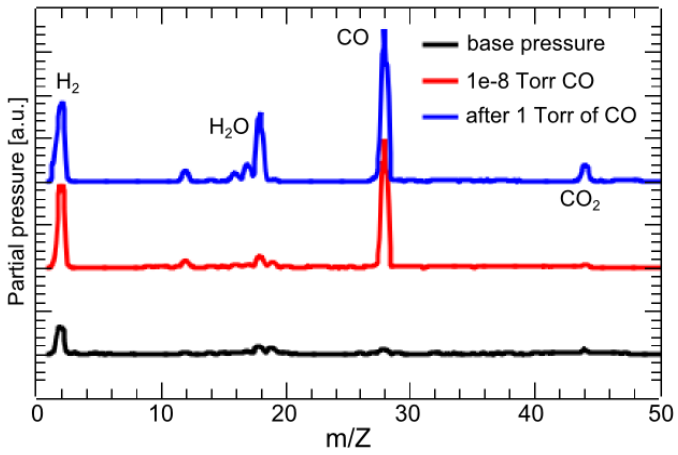


**Fig. S8.** Mass spectrum acquired in the STM chamber at the base pressure of $1\times10^{-10}$ Torr, and reference spectrum under $1\times10^{-8}$ Torr of CO (black and red curves). After the chamber is pumped down to $1\times10^{-8}$ Torr in a few minutes following CO experiments at 1 Torr, residual gases $H_2$, $H_2O$, CO, and $CO_2$, are observed. After a few minutes more, a pressure of $2\times10^{-9}$ was reached (imaging conditions of Fig. 3A) but the partial pressure of $H_2O$ remained unchanged.

**Table S1** Comparative energetics of CO adsorption on hcp ($E_{hcp}$) and fcc ($E_{fcc}$) sites relative to the top sites ($E_{top}$) on Cu(111) surface from different exchange-correlation functionals. Surface slab dimension is 3×3 with thickness of 4 atomic layers. Negative values correspond to lower (more favorable) energies. Bridge configuration of CO adsorption is metastable and transforms to an fcc configuration for all functionals. The PBE+U with U=6 provides the best top-configuration and adsorption energy in agreement with experiment (29, 35-36, 39-40).

| Method | $E_{top}$-$E_{hcp}$, eV | $E_{top}$-$E_{fcc}$, eV | $E_{ads}$(top), eV |
|---|---|---|---|
| LDA | 0.35 | 0.356 | -1.26 |
| PW91 | 0.11 | 0.110 | -0.67 |
| PBE | 0.13 | 0.130 | -0.64 |
| revPBE | 0.04 | 0.042 | -0.40 |
| **PBE+U** | **-0.01** | **-0.02** | **-0.47** |
| PBE-vdW(D2) | 0.19 | 0.21 | 0.76 |
| PBE-vdW(DF) | -0.01 | 0.01 | -0.64 |
| revPBE-vdW(DF) | -0.07 | -0.06 | -0.36 |
| rPW86-vdW(DF2) | -0.14 | -0.13 | -0.33 |

**Table S2** Calculated formation energies of various $Cu_x(CO)_y$ clusters on Cu(111) calculated using the PBE+U approximation, as shown in eq. 1. $E_{ads}$ is the average adsorption energy per peripheral CO molecule on low-coordinated sites (the central CO remains close to -0.47 eV). The energy gain from CO adsorption should be compared to the CO adsorption on the (111) terrace (-0.47 eV).

| Cluster | $E_{Form}$, eV | $E_{ads}$(CO), eV/mol |
|---|---|---|
| CO on (111) | | -0.47 |
| Cu from kink | +0.83 | |
| Cu(CO) | +0.34 | -0.96 |
| $Cu_3$ | +1.64 | |
| $Cu_3(CO)_3$ | +0.26 | -0.93 |
| $Cu_{19}$ | +3.61 | |
| $Cu_{19}(CO)_7$ | +1.45 | -0.83 |
| $Cu_{19}(CO)_{13}$ | -0.59 | -0.82 |
| $Cu_{19}Cu_3$ | +5.39 | |
| $Cu_{19}Cu_3(CO)_9$ | +1.97 | -0.85 |
| $Cu_{19}Cu_3(CO)_{15}$ | -0.21 | -0.84 |

**Table S3** Formation energies of: Cu adatoms from the kink sites, relative to the bulk with and without adsorbed CO; adsorption energies of CO on the flat (111) surface, kink sites; Cu+CO couples in minimum energy configuration on the Cu(111) surface.

| Cluster | $E_{form}$, eV | $E_{ads}$(CO), eV/mol |
|---|---|---|
| CO on terrace site | -0.47 | -0.47 |
| CO on kink site | -0.77 | -0.77 |
| Cu from kink | +0.83 | |
| Cu from surf. vacancy | +1.33 | |
| Cu bulk | +0.82 | |
| Cu+CO from kink | +0.64 | -0.96 |
| Cu+CO from surf. vacancy | +0.83 | -0.96 |
| Cu+CO bulk | +0.34 | -0.96 |

**References**

(33) G. Kresse, J. Furthmuller, Efficient Iterative Schemes for Ab initio Total-Energy Valculations using a Plane-Wave Basis Set. *Phys. Rev. B* **54**, 11169-11186 (1996).
(34) G. Kresse, F. Joubert, From Ultrasoft Pseudopotentials to the Projector Augmented Wave Method. *Phys. Rev. B* **59**, 1758-1775 (1999).
(35) W. Kirstein, B. Krüger, F. Thieme, CO Adsorption Studies on Pure and Ni-Covered Cu(111) Surfaces, *Surf. Sci.* **176**, 505-529 (1986).
(36) I. Boenicke, W. Kirstein, S. Spinzig, F. Thieme, CO Adsorption Studies on a Stepped Cu(111) Surface, *Surf. Sci*. **313**, 231-238 (1994).
(37) V. P. Zhdanova, Ostwald Ripening with Kinetically Limited Bond Formation, *Eur. Phis. J. B* **19**, 97-100 (2001).
(38) J. Bardeen, L. N. Cooper, J. R. Schrieffer, Microscopic Theory of Superconductivity, *Phys. Rev.* **106**, 162-164 (1957).
(39) S. Vollmer, G. Witte, Ch. Wöll, Determination of Site Specific Adsorption Energies of CO on Copper, *Catal. Lett.* **77**, 97-101 (2001).
(40) M. Gajdos, J. Hafner, CO Adsorption on Cu(111) and Cu(001) Surfaces: Improving Site Preferences in DFT Calculations, *Surf Sci.* **590**, 117-126 (2005).
(41) B. Eren, Ch. Heine, H. Bluhm, G. A. Somorjai, M. Salmeron, Catalyst Chemical State during CO Oxidation Reaction on Cu(111) Studied with Ambient Pressure XPS and NEXAFS, J. Am. Chem. Soc. **137,** 11186−11190 (2015).